



Single-nanometer iron oxide nanoparticles as tissue-permeable MRI contrast agents

He Wei^{a,1}, Agata Wiśniowska^{b,1}, Jingxuan Fan^{a,2}, Peter Harvey^{a,2}, Yuanyuan Li^c, Victoria Wu^a, Eric C. Hansen^d, Juanye Zhang^d, Michael G. Kaul^e, Abigail M Frey^a, Gerhard Adam^e, Anatoly I. Frenkel^{c,f}, Mounji G. Bawendi^{d,3}, and Alan Jasanoff^{a,3}

^aDepartment of Biological Engineering, Massachusetts Institute of Technology, Cambridge, MA 02139; ^bHarvard–Massachusetts Institute of Technology Health Sciences & Technology, Massachusetts Institute of Technology, Cambridge, MA 02139; ^cDepartment of Materials Science and Chemical Engineering, Stony Brook University, Stony Brook, NY 11794; ^dDepartment of Chemistry, Massachusetts Institute of Technology, Cambridge, MA 02139; ^eDepartment of Diagnostic and Interventional Radiology and Nuclear Medicine, Center for Radiology and Endoscopy, University Medical Center Hamburg-Eppendorf, Hamburg 20246, Germany; and ^fChemistry Division, Brookhaven National Laboratory, Upton, NY 11973

Contributed by Mounji G. Bawendi, September 8, 2021 (sent for review June 2, 2021; reviewed by Kevin M. Bennett and Shouheng Sun)

Magnetic nanoparticles are robust contrast agents for MRI and often produce particularly strong signal changes per particle. Leveraging these effects to probe cellular- and molecular-level phenomena in tissue can, however, be hindered by the large sizes of typical nanoparticle contrast agents. To address this limitation, we introduce single-nanometer iron oxide (SNIO) particles that exhibit superparamagnetic properties in conjunction with hydrodynamic diameters comparable to small, highly diffusible imaging agents. These particles efficiently brighten the signal in T_1 -weighted MRI, producing per-molecule longitudinal relaxation enhancements over 10 times greater than conventional gadolinium-based contrast agents. We show that SNIOs permeate biological tissue effectively following injection into brain parenchyma or cerebrospinal fluid. We also demonstrate that SNIOs readily enter the brain following ultrasound-induced blood–brain barrier disruption, emulating the performance of a gadolinium agent and providing a basis for future biomedical applications. These results thus demonstrate a platform for MRI probe development that combines advantages of small-molecule imaging agents with the potency of nanoscale materials.

iron oxide nanoparticle | magnetic resonance imaging | molecular imaging | brain

Magnetic nanoparticles can dramatically shorten longitudinal and transverse relaxation times (T_1 and T_2) in MRI, and they consequently produce strong contrast in relaxation-weighted MRI scans (1, 2). There has been considerable interest in harnessing these effects for noninvasive assessment of physiological parameters in living subjects. Magnetic nanoparticles (3) have been functionalized to bind or sense a variety of biologically interesting targets (4), but the large size of most nanoparticles limits their ability to access and probe cellular-level phenomena in tissue. To address this problem, we undertook to create magnetic nanoparticles small enough to effectively permeate parenchyma while still exhibiting high magnetic moments with respect to traditional gadolinium-based MRI contrast agents. We reasoned that such particles could function as an attractive platform for molecular and cellular imaging applications.

To facilitate tissue permeability, nanoparticles should have a size comparable to paramagnetic agents like gadolinium diethylenetriaminepentaacetic acid (Gd-DTPA), which has a molecular diameter of about 1 nm. This would require synthesizing iron oxide–based contrast agents with diameters considerably lower than the smallest previously reported species (5, 6). To accomplish this, we sought to create magnetic single-nanometer iron oxide (SNIO) contrast agents by improving our recently reported magnetic nanoparticle synthesis procedures (6).

Results

SNIO cores were produced from the thermal decomposition of Fe(oleate)₃ in the presence of oleic acid (Fig. 1A). The procedure

was implemented in optimized mixtures of 1-tetradecene and 1-hexadecene using a thermal decomposition temperature of 260 °C that allows the nucleation of organometallic precursors but suppresses the growth of large crystals via Ostwald ripening (7). This was followed by a controlled oxidation with trimethylamine *N*-oxide, which ensures that the particles adopt a relatively stable maghemite structure (8).

The local structure surrounding the iron atoms of the SNIOs was analyzed using extended X-ray absorption fine structure (EXAFS) analysis. The radial distribution function computed from the Fourier transform of the SNIO EXAFS spectrum resembles those of maghemite and magnetite but is dissimilar to data from iron foil and hematite (Fig. 1B), suggesting that SNIOs have an inverse spinel crystal structure like maghemite. The position and shape of the SNIO peak between 2.5 and 3.5 Å are particularly similar to characteristics of the corresponding maghemite peak. The EXAFS data were further analyzed to determine the ratio of octahedral sites to tetrahedral sites in SNIOs (SI Appendix, Fig. S1). Results demonstrate that

Significance

This work shows that iron oxide species as small as 1 nm in diameter can exhibit superparamagnetic properties and act as potent contrast agents for MRI. Because of their small size, the resulting particles effectively permeate dense biological tissue and undergo ultrasound-facilitated delivery from the vasculature to the brain. They also exhibit T_1 -weighted contrast-inducing properties similar to widely used paramagnetic MRI contrast agents but with far higher potency per molecule. Single-nanometer iron oxide agents, therefore, constitute a beneficial basis for the development of molecular imaging probes designed to detect targets in T_1 -weighted MRI. They might also function as alternatives to widely used gadolinium-based MRI agents in clinical contexts where gadolinium-related toxicity is a concern.

Author contributions: H.W., A.W., M.G.B., and A.J. designed research; H.W., A.W., J.F., P.H., Y.L., V.W., E.C.H., J.Z., M.G.K., and A.M.F. performed research; H.W., A.W., J.F., P.H., Y.L., E.C.H., J.Z., M.G.K., and A.M.F. contributed new reagents/analytic tools; H.W., A.W., J.F., P.H., Y.L., V.W., E.C.H., J.Z., M.G.K., A.M.F., A.I.F., M.G.B., and A.J. analyzed data; and H.W., A.W., Y.L., G.A., A.I.F., M.G.B., and A.J. wrote the paper.

Reviewers: K.M.B., Washington University in St. Louis School of Medicine; and S.S., Brown University.

The authors declare no competing interest.

Published under the PNAS license.

¹H.W. and A.W. contributed equally to this work.

²J.F. and P.H. contributed equally to this work.

³To whom correspondence may be addressed. Email: mgb@mit.edu or jasanoff@mit.edu.

This article contains supporting information online at <http://www.pnas.org/lookup/suppl/doi:10.1073/pnas.2102340118/-DCSupplemental>.

Published October 15, 2021.

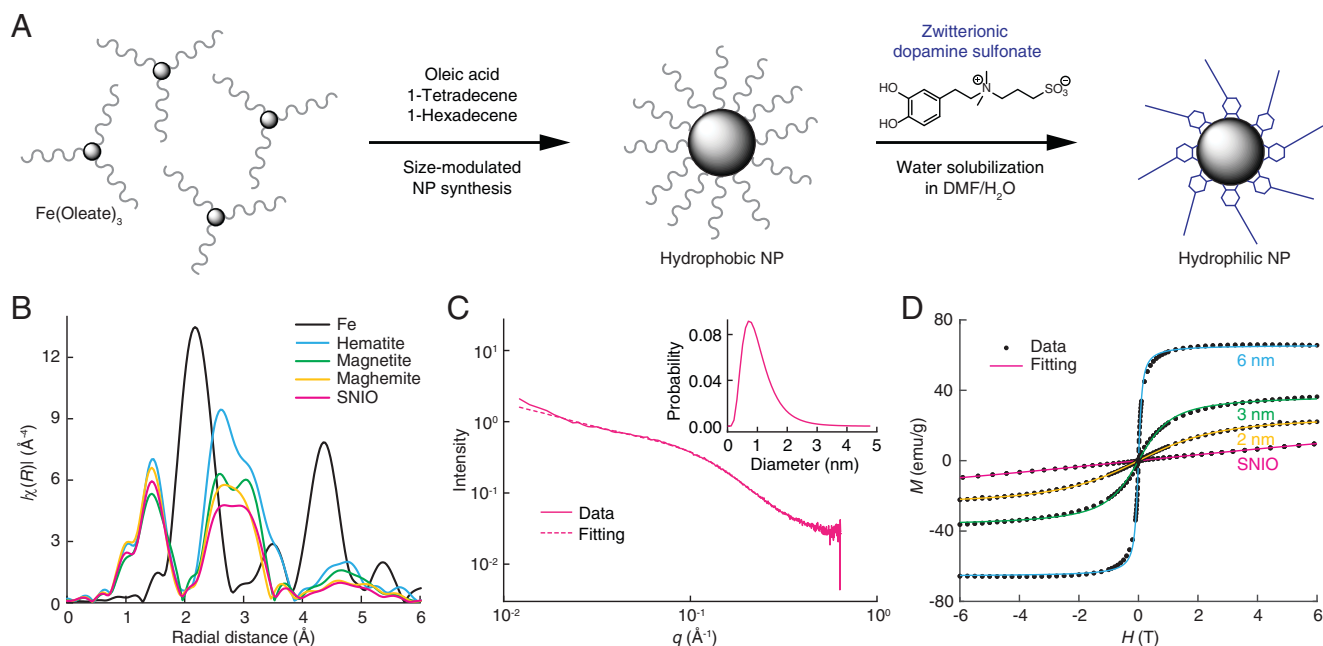


Fig. 1. Synthesis and characterization of SNIOs. (A) Synthesis of ZDS-coated SNIOs. The 3,4-dihydroxyl groups of ZDS ligand bind to the SNIO surface, exposing the hydrophilic zwitterionic side chain to solution and contributing to particle stability in suspension. NP, nanoparticle; DMF, dimethylformamide. (B) EXAFS data from SNIOs and other iron-containing minerals (Fe data are scaled by 50%). (C) SAXS data obtained from a sample of SNIOs over the scattering vector (q) range from 0.009 to 0.5 \AA^{-1} . The dashed curve shows the results of fitting to a spherical scattering model, as described in the text; *Inset* shows the particle diameter distribution corresponding to this fitted curve. (D) M - H curves of SNIO and 2- to 6-nm iron oxide core nanoparticles measured by SQUID magnetometry. Dots indicate experimental measurements, and curves represent Langevin functions fit to the data.

octahedral sites dominate, consistent again with a maghemite-like structure, but that the mean-squared deviations in the Fe-O and Fe-Fe pair distances are larger for SNIOs than for the magnetite and maghemite references (*SI Appendix, Table S1*), indicating the presence of lattice distortions in the SNIO mineral. An X-ray absorption near-edge structure (XANES) spectrum of SNIOs was also obtained (*SI Appendix, Fig. S2*) and could be modeled as a linear combination of the XANES spectra of maghemite (53%) and magnetite (47%). This is again consistent with the conclusion that SNIOs resemble maghemite, albeit with lattice distortions likely arising from the abundance of surface iron atoms.

Due to their small size, we could not clearly visualize SNIOs by transmission electron microscopy (TEM), but we were able to measure their core diameters using small-angle X-ray scattering (SAXS). SAXS results were well approximated (χ^2 goodness of fit test; $\chi^2 = 165$) by a single population of dense spheres of diameter $1.0 \pm 0.5 \text{ nm}$ (mean \pm polydispersity) (Fig. 1C). The SNIO core size was also independently estimated from magnetization data recorded using a superconducting quantum interference device (SQUID) operated at room temperature (Fig. 1D). Data from superparamagnetic iron oxide nanoparticles (SPIONs) with TEM-determined core sizes of 2, 3, and 6 nm were first fit to the Langevin function (9); this resulted in computed diameters of 3.7, 4.4, and 7.5 nm, respectively, implying a mean scaling factor of 1.5 relating the two measures. When magnetometry data from SNIOs were fit and scaled using the same factor, an estimated diameter of 1.3 nm was obtained, consistent with the SAXS results and with the conclusion that SNIOs do indeed possess a mean core size of about 1 nm.

The SNIO magnetization data also predict how these particles will behave in MRI. The absence of hysteresis near zero field, combined with the slightly saturating profile of the M - H curve, indicates that the particles are weakly superparamagnetic. At the same time, the specific magnetization of SNIOs,

measured to be $9.5 \pm 0.5 \text{ emu/(g iron oxide)}$ at 6 T, is much lower than that of 6-nm iron oxide particles (10), $65.6 \pm 0.2 \text{ emu/(g iron oxide)}$, and only somewhat higher than that of paramagnetic Gd-DTPA, $6.40 \pm 0.01 \text{ emu/(g Gd)}$. The similarity between magnetic properties of SNIO and Gd-DTPA suggests that the two compounds should exhibit similar relaxation properties in MRI (11), as reflected by their longitudinal relaxivity (slope of $1/T_1$ vs. concentration, r_1) and transverse relaxivity (slope of $1/T_2$ vs. concentration, r_2).

To measure SNIO relaxivity under biologically relevant conditions, the particles were first solubilized in aqueous medium by exchanging oleic acid for a hydrophilic zwitterionic dopamine sulfonate (ZDS) coating (Fig. 1A) (12). Prior results have demonstrated that this coating preserves magnetic properties, offers long-term stability over a variety of pH and salinity conditions, and minimizes nonspecific interactions with biological components in vitro and in vivo (13). Gel filtration chromatography of ZDS-coated SNIOs reveals an average hydrodynamic diameter (D_h) of $3.1 \pm 0.1 \text{ nm}$ (*SI Appendix, Fig. S3*), indicating that the coating is less than 1 nm thick and adds less than 2 nm to the overall diameter of these particles, consistent with previous studies (12, 13). Longitudinal optical studies of the particles indicate their stability in suspension over a period of weeks (*SI Appendix, Fig. S4*).

When measured at 1.5 T, the solubilized SNIOs display an r_1 of $3.0 \pm 0.2 \text{ (mM Fe)}^{-1} \text{ s}^{-1}$ and an r_2 of $3.4 \pm 0.1 \text{ (mM Fe)}^{-1} \text{ s}^{-1}$ (Table 1 and *SI Appendix, Table S2*). The consequent ratio of r_2/r_1 near unity is similar to that of Gd-DTPA and reflective of unsaturated magnetically active compounds that most effectively enhance contrast in T_1 -weighted MRI. Across a range of fields, values of r_1 for SNIO per metal ion are 20 to 30% lower than r_1 values obtained for Gd-DTPA. This is to be expected given the lower spin number of iron vs. gadolinium atoms and the possibility that ZDS-coated SNIO cores may not offer as many first- or second-sphere sites for water relaxation per metal atom as Gd-DTPA does. Because SNIO particles contain

Table 1. Longitudinal relaxivities of SNIO and Gd-DTPA

Contrast agent	Field strength (T)	Longitudinal relaxivity (r_1)*		
		Per metal atom ($\text{mM}^{-1} \text{s}^{-1}$)	Per molecule [†] ($\text{mM}^{-1} \text{s}^{-1}$)	Per volume [‡] ($\text{mM}^{-1} \text{s}^{-1} \text{nm}^{-3}$)
SNIO	1.5	3.0	60	3.8
SNIO	7.0	4.9	98	6.3
Gd-DTPA	1.5	4.8	4.8	1.6
Gd-DTPA	7.0	4.1	4.1	1.3

* Values are measured at room temperature in PBS.

[†] Assumes 20 Fe atoms per SNIO, inferred from measured core size values by SAXS.

[‡] Per metal atom values normalized by 15.6 nm^3 (SNIO) or 3.05 nm^3 (Gd-DTPA).

~ 20 iron atoms each, however, their per-particle r_1 values of $\sim 60 \text{ (mM particle)}^{-1} \text{ s}^{-1}$ are ~ 13 times higher than the Gd-DTPA value of $4.8 \text{ mM}^{-1} \text{ s}^{-1}$. Because ZDS-coated SNIOs have about twice the diameter of Gd-DTPA, their greater relaxivity also corresponds to a substantially higher T_1 -weighted MRI effect per unit of volume occupied by the contrast agent (14), approximately equal to $3.8 \text{ mM}^{-1} \text{ s}^{-1} \text{ nm}^{-3}$ for SNIO vs. $1.6 \text{ mM}^{-1} \text{ s}^{-1} \text{ nm}^{-3}$ for Gd-DTPA.

The small size of SNIO contrast agents enables them to permeate effectively through tissue. As an initial demonstration of this capability, we began by comparing the convective spreading of SNIOs with that of larger, previously reported lipid-coated iron oxide (LCIO) contrast agents (15) with mean $D_h = 35 \pm 1 \text{ nm}$. The extent of spreading was determined by computing the full width at half-maximum (FWHM) of MRI signal changes induced by intraparenchymal injection of $7.2 \mu\text{L}$ of each agent, based on images that display both T_2 contrast from the LCIO particles and T_1 contrast from the SNIO agents simultaneously (Fig. 2A). The results reveal FWHM values of 1.9 ± 0.1 and $1.2 \pm 0.2 \text{ mm}$ for SNIO and LCIO nanoparticles, respectively (Fig. 2B), indicating that brain tissue is significantly more permeable (t test; $P = 0.02$, $n = 3$) to the smaller particles.

As a further demonstration of the ability of SNIO contrast agents to spread effectively throughout the brain, we infused a $50\text{-}\mu\text{L}$ volume of SNIOs at 50 mM Fe concentration into the cisterna magna (16), a prominent cerebrospinal fluid reservoir behind the cerebellum, and measured resulting changes in the T_1 -weighted MRI signal (Fig. 3A) and longitudinal relaxation rates ($R_1 = 1/T_1$) at each voxel in sagittal brain slices of three rats (Fig. 3B). This analysis showed that $85 \pm 6\%$ of brain pixels experienced R_1 increases of 10% or more and $71 \pm 6\%$ experienced increases of 25% or more (Fig. 3C), indicating that

virtually the entire brain can be labeled to some extent using this procedure. To determine further whether SNIOs infused via the cisterna magna spread on a microscopic scale, we analyzed postmortem brain sections from injected animals by Prussian blue histology (Fig. 3D). The results demonstrate that SNIO particles can permeate parenchymal tissue far from cerebrospinal fluid reservoirs in both cortical and subcortical regions of the brain.

Comparison of the SNIO r_1 value of $66 \text{ (mM particle)}^{-1} \text{ s}^{-1}$ at 9.4 T with the noise level of the R_1 maps of Fig. 3 permits an estimation of the limit of detection for SNIOs under the acquisition conditions applied here. The mean SD of cortical R_1 measurements across three animals is 0.031 s^{-1} , implying that a minimum concentration of about $0.9 \mu\text{M}$ SNIO particles could be detected with statistical significance of $P \leq 0.05$ in a Z test based on R_1 . Because signal-to-noise ratio can easily be improved through averaging or resolution adjustment, detection of yet lower SNIO levels in R_1 maps or T_1 -weighted MRI could be attained straightforwardly with adjusted acquisition parameters. The SNIOs are not, however, as readily detectable in R_2 maps. Under acquisition conditions closely analogous to those in Fig. 3, R_2 values are measured with an average SD of 1.6 s^{-1} ($n = 3$), implying that a concentration of more than $20 \mu\text{M}$ SNIO particles would be required for statistically significant detection based on their r_2 values.

One of the most common applications of small-molecule MRI contrast agents in neurology involves their application for assessment of blood–brain barrier (BBB) integrity in conditions such as stroke and traumatic brain injury. In such applications, contrast agents are injected intravenously; in areas where the BBB is compromised, the agents leak into the brain and accumulate, allowing subsequent detection by T_1 -weighted imaging. The small size and permeability of SNIOs in brain tissue suggest that these contrast agents could also provide such indications of BBB disruption. To test this idea, we first determined the ability of SNIOs to persist in the vasculature by measuring their circulation time in pilot experiments in mice (SI Appendix, Fig. S5). These experiments demonstrated vascular contrast enhancement of SNIO with a blood half-life of about 2 min; this is somewhat lower than analogous half-lives reported for Gd-DTPA in rodents (17, 18) and of possible advantage when trying to distinguish cerebral contrast enhancement from residual contrast changes in blood. Biodistribution analysis (SI Appendix, Fig. S6) shows that the intravenously (IV) injected SNIOs exhibit half-lives of about 2 min in the heart and 19 min in the liver and kidney. According to allometric scaling principles, these values in mice correspond to predicted half-lives of 11 and 95 min in rats (19). Contrast returned to baseline in the heart, liver, and kidney within 1 h but continued developing in the bladder over time, again indicating efficient renal clearance of SNIOs.

To probe the ability of SNIO nanoparticles to assess compromised BBB function, we used unfocused transcranial ultrasound (20, 21) to create widespread BBB disruptions targeted

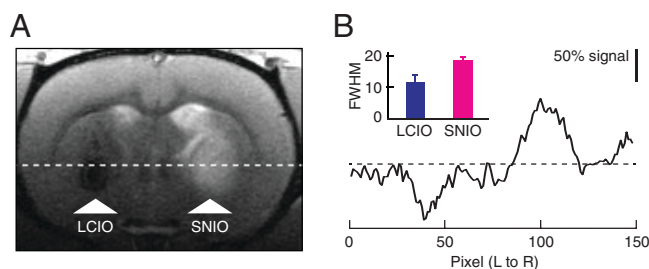


Fig. 2. Contrast induced by nanoparticle injections into brain parenchyma. (A) A representative MRI scan obtained after injection of SNIOs and larger iron oxide nanoparticles (LCIOs) into the striatum of a rat. A coronal scan is shown with injection sites labeled (arrowheads), indicating hypointensity for LCIOs and hyperintensity for SNIOs. (B) A cross-section, left to right (L to R) through the same image corresponding to the position of the horizontal line in A. Normalized intensities (scale bar) are indicated with respect to baseline (dashed line). Inset shows the mean and SEM of FWHM values measured for LCIO and SNIO injections into three animals each. Error bars denote SEM.

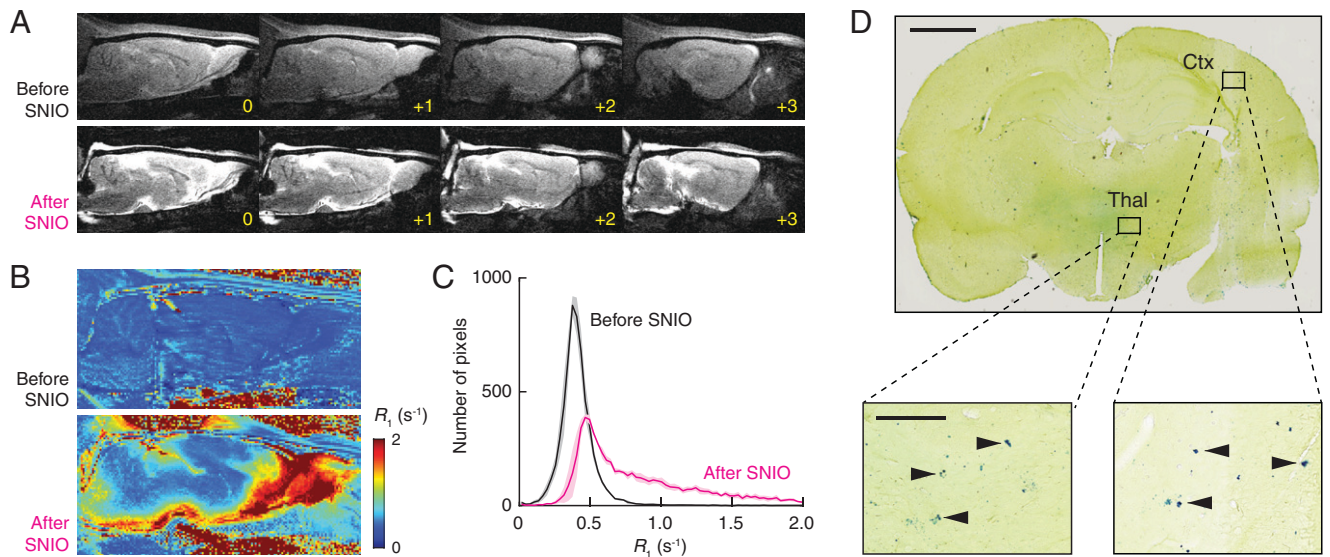


Fig. 3. Brain distribution following intracisternal delivery of SNIOs. (A) T_1 -weighted MRI scans of a representative animal indicating contrast before (Upper) and after (Lower) infusion of 50 μ L SNIOs (50 mM Fe) into the cisterna magna of the rat ventricular system. Four sagittal slices are shown in each case, with yellow labels denoting the position in millimeters with respect to the midline. (B) Sagittal R_1 maps obtained from the same animal before (Upper) and after (Lower) intracisternal SNIO delivery. (C) Mean histograms of pixel intensity before and after intracisternal infusion in three animals, consistent with the broad contrast and R_1 enhancements in A and B. Shading denotes SEM. (D, Upper) Prussian blue histochemical visualization of parenchymal iron introduced by intracisternal SNIO delivery. Close-up views (D, Lower) display regions of thalamus (Thal) and cortex (Ctx), with arrowheads indicating individual iron-containing deposits. (Scale bars: D, Upper, 2 mm; D, Lower, 200 μ m.)

to the right hemisphere of rat brains and compared the visualization of these disruptions using SNIO and Gd-DTPA contrast agents (Fig. 4A). Sonication was applied following intravenous infusion of microbubbles to induce transient BBB opening. Subsequently, there was a roughly 1-h time window of BBB opening during which agents were injected at equivalent intravascular doses (1 mL containing 50 mM Fe or Gd). This procedure produced contrast changes consistent with placement of the ultrasound transducer and its effective focal width of 5 mm (Fig. 4B). When comparing MRI scans obtained 5 min before vs. 15 to 20 min after contrast agent infusion, mean image signal enhancements could be observed throughout much of the brain in cohorts of sonicated animals injected with SNIOs or Gd-DTPA but less so in unsonicated animals injected with SNIOs (Fig. 4C) (all $n = 4$). Maps of mean signal change observed during the 20 min after the end of the contrast agent infusion period show even starker discrepancies between sonicated vs. unsonicated animals (SI Appendix, Fig. S7), likely due to reduced contributions from intravascular concentration changes during this period. Histological analysis indicates little disruption to the tissue following sonication and SNIO delivery (SI Appendix, Fig. S8), suggesting that neither the particles nor the delivery procedure are acutely toxic.

The volume of cerebral MRI contrast enhancement detected using SNIOs was similar to that detected using Gd-DTPA (Fig. 4D). The average magnitude of signal changes measured using gadolinium was about twice as high, however, with mean enhancements of $49 \pm 3\%$ and $28 \pm 2\%$ observed for Gd-DTPA and SNIO, respectively (Fig. 4E). When scaled by the relaxivities of the two agents, the difference between results is still not fully accounted for. This suggests that SNIOs are somewhat less effective at crossing lesioned BBB areas, probably due to their somewhat larger D_h compared with the reported value of 1.8 nm for Gd-DTPA (22), which is presumably more favorable for BBB permeation. With respect to their molecular concentrations, however, SNIOs are roughly 10 times more effective than Gd-DTPA at producing brain contrast changes following ultrasound-mediated BBB opening, with

observed mean signal enhancements of about 11% per millimolar injected SNIO particles vs. $\sim 1\%$ per millimolar Gd-DTPA molecules injected. These results show how the small size and high relaxivity of SNIO nanoparticles facilitate effective trans-BBB permeation and detection of BBB disruptions using T_1 -weighted MRI in living animals.

Discussion

We have demonstrated that iron oxide nanoparticles with diameters of about 1 nm can be synthesized using modified thermal decomposition methods and that they display superparamagnetic qualities and maghemite-like crystal morphology, despite their small size. The resulting SNIO species act as effective contrast agents for MRI, where they combine the small size and tissue permeability of small paramagnetic MRI agents with per-molecule T_1 relaxivity over an order of magnitude higher than conventional contrast agents (23). The SNIO particles were shown to spread effectively following intracranial injection into brain parenchyma or cerebrospinal fluid, bypassing one of the principal limitations of larger nanoparticle imaging agents. SNIOs also permeate the brain from the vasculature following ultrasound-mediated BBB disruption, a model of BBB dysfunction in various neurological conditions (24) and a clinically applicable technique for noninvasive delivery of exogenous agents to the brain (25). Our results, therefore, introduce a nanostructured material with potential utility across a range of biomedical MRI applications.

Although iron oxide contrast agents are not generally known for displaying high T_1 contrast in MRI, SNIOs accomplish this effectively because of their low magnetic saturation at relevant imaging field strengths. This enables SNIOs to exhibit relatively high r_1 values, as well as r_2/r_1 ratios near unity, similar to small mononuclear complexes of gadolinium, manganese, and iron (26). Because SNIOs contain many metal atoms per particle, their per-molecule longitudinal relaxivities are substantially greater; each SNIO particle exhibits 13- and 24-fold higher r_1 than each molecule of Gd-DTPA at 1.5 and 7 T, respectively

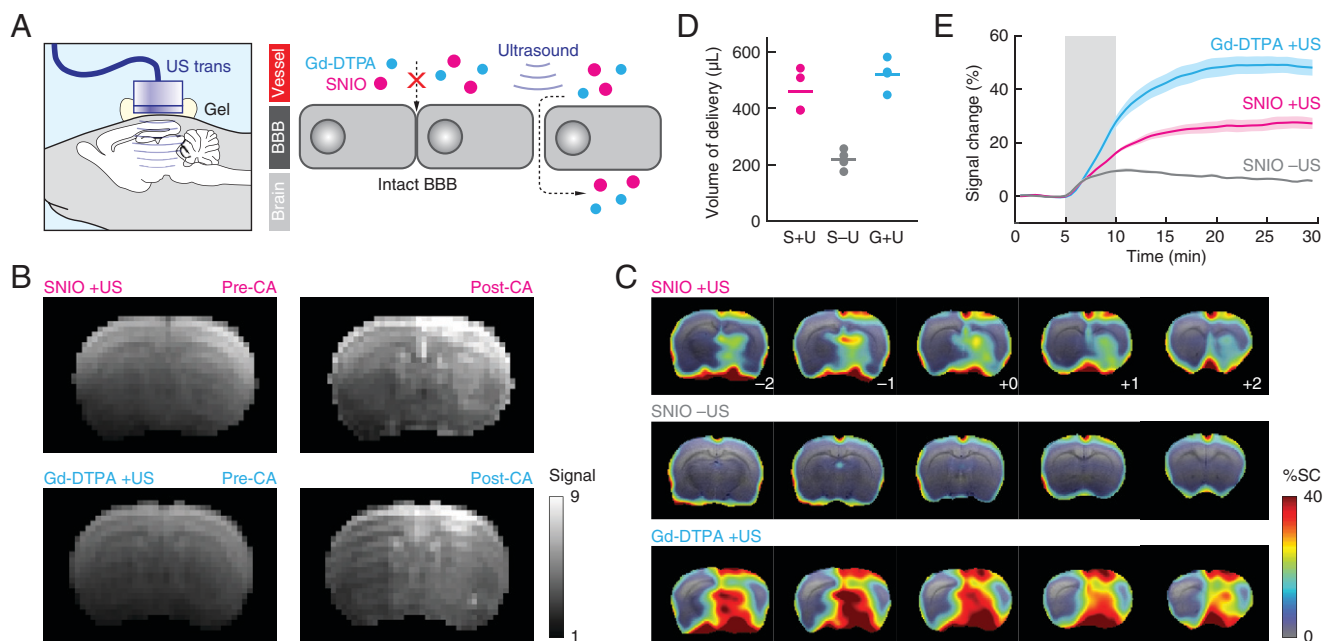


Fig. 4. Detection of BBB opening using SNIO agents. (A) Application of unfocused transcranial ultrasound (US) (Left) disrupts junctions between cells that make up the BBB, allowing contrast agents (CAs) to enter and accumulate in the brain (Right). (B) T_1 -weighted coronal images of representative individual animals that received ultrasound treatment followed by IV infusion of SNIOs (Upper) or Gd-DTPA (Lower). In each case, images before CA injection (pre-CA; Left) and after injection (post-CA; Right) are shown. (C) Mean percentage signal changes (% SCs; color) observed after contrast agent infusion, with respect to preinjection signal, in groups of animals ($n = 4$) that underwent SNIO injection after ultrasound (Top), SNIO injection without ultrasound (Middle), or Gd-DTPA infusion after ultrasound (Bottom). Five brain sections are shown in each case, corresponding to coronal slices from bregma -2.0 to $+2.0$ mm. The underlay is a T_2 -weighted anatomical scan. (D) Brain volumes displaying contrast enhancement over 10% following treatment with SNIOs after US (S + U), SNIOs without US (S - U), and Gd-DTPA after US (G + U), where S, U, and G represent SNIOs, ultrasound, and Gd-DTPA, respectively. (E) Time courses of signal changes observed in regions of peak mean signal change under the three experimental conditions. Shading represents SEM of $n = 4$. Ultrasound was delivered ~ 45 min prior to data acquisition; the gray box denotes the period during which SNIO or Gd-DTPA solutions were infused.

(Table 1). This allows SNIOs to be detected at concentrations over an order of magnitude lower than typical paramagnetic contrast agents. Whereas paramagnetic agents are rarely detectable *in vivo* below $10 \mu\text{M}$ levels (27), SNIOs should be detectable at submicromolar concentrations, comparable to those of potential molecular imaging targets such as signaling molecules (28, 29). Larger iron oxide nanoparticles can be detected at even lower particle concentrations, but they predominantly produce negative T_2 -dependent contrast that is considered disadvantageous in some contexts (30). Larger SPIONs also display poor permeability in biological tissue (31), restricting their capabilities for targeted molecular imaging applications. Compared with most SPION molecular imaging agents, the high tissue permeability and brain delivery capabilities we demonstrated for SNIOs, therefore, provide potentially crucial advantages because they can help these particles reach analytes in any part of the body.

Although we did not target SNIO agents to specific molecules here, such applications could be implemented by modifying the particle surface to permit conjugation to binding or sensing moieties (32). In our prior studies, a polyethylene glycol (PEG)-modified catechol ligand containing a thiol group was mixed with ZDS ligands to coat 8-nm SPIONs, followed by conjugation to streptavidin-maleimide and subsequent labeling of biotinylated targets (12). Although the specific PEGylated catechol we used is also expected to bind SNIO cores, its 600-Da PEG chain would add substantially to the D_h of solubilized SNIOs, compromising some of the benefits that come from the small size of these particles. For future work, more compact catechol derivatives containing thiols or other reactive groups (33) could be used instead. Functionalized SNIOs could then be conjugated to species such as peptides, aptamers, or

antibodies (34–36) to enable a variety of targeted MRI applications in the brain or peripheral organs. Conjugation could alter SNIO relaxivity, although it is difficult to anticipate what specific effects would be observed. SNIOs functionalized with large macromolecules would also exhibit higher D_h values and generally lower tissue permeability than the unmodified particles studied here. Even for larger conjugates, however, the small size of SNIOs could prove advantageous for molecular imaging applications because the particles would cause minimal disruption to the binding properties of the molecules used to modify or target them.

SNIO contrast agents could also provide advantages for applications that do not involve molecular-level targeting. In particular, SNIOs could be used as alternatives to paramagnetic T_1 -weighted MRI agents in contexts where heavy metal toxicity induced by conventional agents might otherwise be problematic. SNIOs would not contribute to pathologies associated with some gadolinium-based agents, such as nephrogenic systemic fibrosis (37) and Gd deposition in the human brain (38, 39). Although we have not formally studied the toxicity profile of SNIOs yet, other iron oxide contrast agents are known to be well tolerated (40), and we expect that SNIOs will behave similarly; our own results moreover demonstrated absence of acute toxicity following brain delivery. The comparatively short half-life of SNIOs in the bloodstream reduces exposure to the agents after injection and could be advantageous for reducing potential toxicity as well. The small size and chemical features of SNIOs could enable them to undergo biodistribution patterns conducive to applications in multiple parts of the body. Notably, we have already demonstrated the ability of SNIOs to substitute for Gd-DTPA in the detection of BBB lesions, an important clinical use case for gadolinium-based agents. This

example begins to illustrate how the attractive physical, biochemical, and pharmacokinetic characteristics of SNIO imaging agents could lead to diagnostic utility across a broad range of contexts.

Materials and Methods

Synthesis of Iron Oxide Nanoparticles. Nine hundred milligrams of Fe(oleate)₃ was added to a mixture of 4 mL 1-tetradecene and 1 mL 1-hexadecene in the presence of 190 μL oleic acid at room temperature. This reaction mixture was then degassed at 100 °C under vacuum for 1 h. Afterward, the reaction mixture was rapidly heated to 260 °C for thermal decomposition of Fe(oleate)₃ and incubated at this temperature for 40 min. Upon completion of the reaction, the mixture was allowed to cool down to room temperature, and 113 mg of (CH₃)₃NO oxidizing agent was added. The temperature was then elevated to 130 °C for the oxidation process to complete. After the mixture was cooled to room temperature, an acetone and ethanol solvent mixture (5:3, vol/vol) was added, and the resulting solution was centrifuged at 10,000 × *g* for 10 min. Finally, the supernatant was discarded, and the SNIO pellets were dispersed and stored in 3 mL hexane. The native oleic acid ligand of SNIOs was then exchanged by 2-[2-(2-methoxyethoxy)ethoxy]acetic acid in methanol solvent at 70 °C for 5 h and next by ZDS in the solvent mixture of dimethylformamide/water (2:1, vol/vol) at 70 °C for 12 h (12). Solution stability of the resulting particles was verified by comparing optical absorbance measurements from an ~0.65 μM concentration of SNIO particles in phosphate-buffered saline (PBS) monitored by ultraviolet (UV)-visible spectroscopy using a Varian Cary 5000 UV-Vis-NIR (now part of Agilent Technologies) spectrophotometer (12).

Larger iron oxide nanoparticles with diameters of 2 and 3 nm were prepared by similar methods in long-chain fatty acids at slightly higher temperatures (6). Six-nanometer iron oxide nanoparticles were obtained as a commercial preparation (Ferumoxytol; AMAG Pharmaceuticals, Inc.). LCIO nanoparticles were prepared by mixing commercial 12-nm iron oxide nanoparticles (Ocean NanoTech), L-α-phosphatidylcholine (Avanti Polar Lipids), and L-α-phosphatidylserine (Avanti Polar Lipids), followed by sonication.

X-Ray Scattering Analysis. SAXS data were collected in a scattering vector (*q*) range from 0.009 to 0.50 Å⁻¹ in transmission mode using incident X-rays corresponding to the Cu Kα emission wavelength at 1.5418 Å on a SAXSLAB system (Skovlunde) comprising a Rigaku 002 Microfocus X-ray source (Rigaku Corporation), Osmic staggered parabolic multilayer optics (Rigaku Corporation), and a Dectris PILATUS3 R 300K detector (Dectris USA, Inc.). SNIO cores in hexane were loaded into 1.5-mm quartz capillaries (Hampton Research), which were then sealed with wax. Background signal from hexane was also collected and subtracted from the SNIO data.

Scattering intensity (*I*) vs. *q* data were processed on SasView5 software (<https://www.sasview.org/>) and fit to a scattering model in which scattering objects (i.e., SNIO particles) are treated as dense spheres with a uniform scattering length density, in conjunction with a fractal function for the low *q* range that reflects the contribution of interparticle interactions among adjacent SNIOs in a dense population (41, 42):

$$I_{\text{sphere}}(q) = \frac{\text{scale}}{V} \left[3V(\Delta\rho) \frac{\sin(qr) - qr\cos(qr)}{(qr)^3} \right]^2 \quad [1]$$

$$I_{\text{fractal}}(q) = \varphi V(\Delta\rho)^2 P(q) S(q) \quad [2]$$

$$I_{\text{total}}(q) = I_{\text{sphere}}(q) + I_{\text{fractal}}(q) + \text{background}. \quad [3]$$

Here, the scale is a unitless volume fraction, *V* is the volume of each spherical scattering object (angstroms cubed), *r* is the radius of the sphere (angstroms), Δρ is the difference between the scattering length densities of the maghemite sample (38.5 × 10⁻⁶ Å⁻²) and hexane solvent (6.5 × 10⁻⁶ Å⁻²), φ is the volume fraction of the spherical particles, *P*(*q*) is the scattering from spherical particles that are randomly distributed, *S*(*q*) is the interference from particles organized in fractal-like clusters, and *background* refers to the background intensity level of measurement (centimeters⁻¹ sr⁻¹), where sr stands for steradian.

A log-normal distribution was then introduced to describe the distribution of particle radius (43):

$$f(r) = \frac{1}{\text{Norm}} \frac{1}{r\sigma} e^{-\frac{1}{2}\left(\frac{\ln r - \mu}{\sigma}\right)^2}, \quad [4]$$

where Norm is a normalization constant, *r* is the radius of the spherical particles, and σ denotes the sample's polydispersity. This log-normal distribution gives rise to a mean radius value of $e^{\mu + \frac{\sigma^2}{2}}$, which is used to determine the mean diameter reported in the text.

X-Ray Absorption Analysis. EXAFS data at the Fe K edge were obtained at beamline 7-BM (Quick X-ray Absorption and Scattering, QAS) at the National Synchrotron Light Source II, Brookhaven National Laboratory. The storage ring was operated at an energy of 3.0 GeV and a current of 500 mA. The synchrotron radiation was monochromatized by a channel-cut (111) Si monochromator. The higher harmonics were eliminated by detuning the second monochromator crystal. EXAFS spectra of the sample and references (bulk Fe, hematite, magnetite, and maghemite) were collected in transmission mode. For the measurements, the powders were spread onto adhesive tape, which was then folded and mounted to the sample stage. XANES data from SNIOs were fit to a linear combination of reference data from maghemite and magnetite to estimate their relative contents.

EXAFS analysis was performed as follows. First, the amplitude factor (*S*₀²) was obtained by fitting magnetite (Fe₃O₄) and maghemite (γ-Fe₂O₃) data. Both magnetite and maghemite take inverse spinel structure, in which octahedral Fe sites and tetrahedral Fe sites coexist. In magnetite structure, there are 2/3 octahedral sites and 1/3 tetrahedral sites. In maghemite structure, there are 5/8 octahedral sites and 3/8 tetrahedral sites. At octahedral iron sites, the Fe ion coordinates with six O atoms at the first shell, six octahedral Fe centers at the second shell, and six tetrahedral Fe centers at the third shell. At tetrahedral iron sites, the Fe ion coordinates with 4 O atoms at the first shell, 12 octahedral Fe centers at the second shell, and 4 tetrahedral Fe centers at the third shell. The following parameters were varied in the fit: a single correction to the photoelectron energy origin (Δ*E*₀) for all photoelectron paths, distances (*R*), and their mean square disorder (σ²) values for Fe–O (a unique set of these variables for the octahedrally and tetrahedrally coordinated Fe ions was used) and Fe–Fe (octahedral–octahedral, octahedral–tetrahedral, and tetrahedral–tetrahedral). Coordination numbers were fixed, as dictated by the inverse spinel structure. For analysis of the SNIO sample, the amplitude factor was fixed to the value obtained for the analysis of magnetite and maghemite data. The coordination numbers were fixed to those expected for the octahedral and tetrahedral sites, but their mixing fractions were now variables, constrained by a requirement that they add up to one. The fitting *k* range was 2 to 12 Å⁻¹, and the *R* range was 1 to 4 Å. The fitting *k* weight was three.

Gel Filtration Chromatography. Gel filtration chromatography calibration and measurements were performed using a Superose 6 (GE Healthcare) size-exclusion column. The size-exclusion column was calibrated by protein standards (Bio-Rad) including gamma globulin (hydrodynamic diameter, *D*_h = 11.1 nm), ovalbumin (*D*_h = 6.1 nm), myoglobin (*D*_h = 3.8 nm), and vitamin B₁₂ (*D*_h = 1.67 nm). The relationship between retention time (*t*; minutes) and *D*_h (nanometers) on this column is found to be *D*_h = 68.043 – 2.944 × *t* + 0.0326 × *t*², with uncertainty Δ*D*_h = ±|8.4516 – 0.4833 × *t* + 0.00678 × *t*²|. The peak retention time of 38.4 min for SNIOs thus corresponds to a *D*_h of 3.1 ± 0.1 nm.

SQUID Magnetometry. Magnetic moments (*M*) were measured on MPMS superconducting quantum interference device (SQUID) magnetometers (Quantum Design) using the direct current scanning mode. Sample temperature was kept at 298 K, and the magnetic field (*H*) was swept for two cycles between –6 and 6 T; values of *M* were measured at each *H* value.

The *M*–*H* curve measured by SQUID for superparamagnetic nanoparticles is expected to follow the Langevin function:

$$M = M_s \times \left[\coth\left(\frac{\mu_p H}{k_B T}\right) - \frac{k_B T}{\mu_p} \times \frac{1}{H} \right], \quad [5]$$

where *M*_s is the saturation magnetization, *H* is the field strength, μ_p is the magnetic moment per nanoparticle, *k*_B is the Boltzmann constant, and *T* is the absolute temperature, all in the International System of Units. For spherical nanoparticles, the magnetic moment per nanoparticle is computed using the following formula:

$$\mu_p = M_s \times m_p = \frac{\rho M_s \pi D^3}{6}, \quad [6]$$

where *m*_p is the mass, ρ is the density, and *D* is the diameter of the nanoparticle. These equations were fit to the *M*–*H* curves from each nanoparticle and used to estimate the core diameters of each species.

Relaxivity Measurements. Longitudinal and transverse relaxivities (*r*₁ and *r*₂) were measured using a 1.5-T benchtop relaxometer (Minispec mq60; Bruker) and using measurements acquired on 7-T Bruker MRI scanners. For measurements at 7 T, a rapid acquisition with refocused echoes (RARE, with RARE factor = 2) pulse sequence was used (echo time *TE* = 10, 30, 50, 70, and 90 ms; repetition time *TR* = 120, 150, 250, 500, 1,000, 1,500, 3,000, and 5,000 ms). Data obtained at 7 T were fit to an equation of the form *S* = *k*(1 – exp[–*TR*/*T*₁]) × exp[–*TE*/*T*₂], where *S* is the MRI signal, *k* is a constant of proportionality, and

T_1 and T_2 are the longitudinal and transverse relaxation times, respectively. Relaxivity values were then obtained by linear fitting to graphs of relaxation rates as a function of contrast agent concentration (c) over a range from 0.2 to 1.7 μM Fe, according to the equation " $1/T_i = 1/T_{i0} + r_i c$ ", where $i = 1, 2$ and T_{i0} denotes relaxation rates in the absence of contrast agent. Curve fitting was performed using custom scripts in MATLAB (Mathworks).

Animal Procedures. At the Massachusetts Institute of Technology (MIT), all animal procedures were conducted in accordance with NIH guidelines and with the approval of the MIT Committee on Animal Care. All experiments were performed with male Sprague-Dawley rats, age 5 to 6 wk, supplied by Charles River Laboratories. In the University Medical Center Hamburg-Eppendorf, all mice were also studied in accordance with approved institutional protocols.

Biokinetic Experiments. Prior to the administration of contrast agent, mice were anesthetized by inhalation of a mixture of oxygen and isoflurane and monitored by MRI using a 7-T scanner (Bruker) over a 10-min baseline period. Then, a bolus of 100 μL SNIO solution at a concentration of 50 mM Fe was injected through the tail vein into mice, during continuous scanning. Pulse sequence and scanning parameters followed previously established conditions (6). Regions of interest (ROIs) were drawn on the heart, liver, kidney, and bladder. Mean MRI signal intensities in these ROIs were extracted at each time point and converted to units of percentage signal change with respect to baseline, yielding the data in *SI Appendix, Fig. S6*. Approximate $t_{1/2}$ values were reported as half-times needed for returning to the baseline following SNIO injection.

Intraparenchymal Infusion Experiments. Thirty-three-gauge metal injection cannulae (PlasticsOne) were bilaterally targeted to the striatum 1 mm anterior, 3 mm lateral, and 5.5 mm ventral to bregma. SNIO and LCIO suspensions, both 1 mM in Fe, were infused into opposite hemispheres at a rate of 0.12 $\mu\text{L}/\text{min}$ for 60 min with a remote infuse/withdraw dual-syringe pump. Upon the completion of infusion, cannulae were removed, and each rat was placed in a custom animal holder with a four-channel surface coil mounted over the animal's head. The animal was then transferred into a 9.4-T Biospec MRI scanner (Bruker) equipped with a birdcage volume coil (Bruker) for radiofrequency transmission.

High-resolution anatomical scans of each animal ($n = 3$ rats) were obtained using a fast low-angle shot (FLASH) pulse sequence with $TE = 4$ ms, $TR = 188$ ms, spatial resolution $100 \mu\text{m} \times 100 \mu\text{m} \times 1$ mm, and matrix size 300×175 with 12 slices. Images were visualized in MATLAB, and a rat brain atlas was used as a reference to determine the depth at which nanoparticles were injected. Lines of interest were then drawn across the images at the level of injection. The intensity of pixels along this line was plotted, permitting comparison of the effect of LCIO nanoparticles on the left side of the brain with SNIO nanoparticles on the right side of the brain. FWHMs for each injection site were then computed and plotted.

Cisterna Magna Infusion Experiments. A 1-mm incision was made on the atlanto-occipital membrane between the skull and C1 vertebrae to gain access to the cisterna magna. The incision was washed four times with sterile Gibco Dulbecco's phosphate-buffered saline (DPBS) $1 \times$ (Thermo Fischer) to remove excess blood and cerebrospinal fluid (CSF). A 28-gauge plastic injection cannula (PlasticsOne) was implanted through the incision and secured by tissue glue. A remote infuse/withdraw dual-syringe pump was used to infuse SNIO (50 mM Fe) fluid at a rate of 5 $\mu\text{L}/\text{min}$ for 10 min at a depth of 1.5 mm. Upon the completion of infusion, the cannula was left in place for an additional 5 min before removal. The incision was closed using tissue glue and tissue cement. The rats were recovered under 1.5% isoflurane for ~ 30 min, and then, they were placed in a custom animal holder with a four-channel surface coil mounted over the animal's head. The rat was next transferred into a 9.4-T Biospec MRI scanner (Bruker) equipped with a birdcage volume coil (Bruker) for radiofrequency transmission. As shown in Fig. 3A, high-resolution anatomical scans of each animal ($n = 3$ rats) before and after cannula implantation and SNIO injection were obtained separately using a FLASH pulse sequence with $TE = 4$ ms, $TR = 171$ ms, spatial resolution $100 \mu\text{m} \times 100 \mu\text{m} \times 1$ mm, and matrix size 300×175 with eight slices.

A high-resolution T_1 map of each animal ($n = 3$ rats) was obtained using a RARE pulse sequence with $TE = 10$ ms; $TR = 120, 150, 250, 500, 1,000, 1,500, 3,000,$ and $5,000$ ms; RARE factor 2; spatial resolution $200 \mu\text{m} \times 200 \mu\text{m} \times 1$ mm; and matrix size 150×75 with one slice. Analogous R_2 maps were obtained from an identical acquisition but with $TR = 3,000$ ms and $TE = 10, 30, 50, 70, 90, 110, 130,$ and 150 ms. Data obtained before and after SNIO injection were imported from the Bruker Paravision software and then converted into R_1 maps using MATLAB. Brain tissue was manually segmented away from nonbrain areas, and analysis of relaxation rates in the brain voxels was performed using image processing routines in MATLAB. Limits of

detection under T_1 - or T_2 -weighted imaging were estimated by computing the mean SD of per-voxel signal among three animals and determining the concentration of SNIO agents required to achieve an R_1 or R_2 change of 1.96 times the mean SD. Such concentrations would be detectable as significant differences ($P \leq 0.05$) under Z tests of relaxation rates with respect to baseline. These calculations were based on r_1 and r_2 values of 3.3 and 7.1 (mM Fe) $^{-1} \text{s}^{-1}$, respectively, measured for SNIOs at 9.4 T and room temperature.

Prussian Blue Staining. To visualize contrast agent distribution after cisterna magna injection, animals were transcidentally perfused with PBS followed by 4% paraformaldehyde in PBS. Brains were extracted, postfixed overnight at 4°C, and sectioned within a week. Sections were incubated in Prussian blue working solution (5% potassium ferrocyanide and 2% hydrochloric acid, 1:1, vol/vol) for 30 min. Tissue was then removed from the stain and rinsed with water and 100% ethanol in succession. Treated brain sections were then mounted onto glass slides and imaged by bright-field microscopy.

Ultrasound-Mediated BBB Disruption. Rats were anesthetized with 2% isoflurane and then underwent the placement of the tail vein catheter for microbubble injection and contrast agent delivery in the MRI scanner. The tail vein was visualized by application of alcohol to the skin of the tail, and a catheter (24G Surflo; Terumo) was slowly inserted into the vein until obvious blood backflow was observed. The catheter was secured to the tail by placing a tongue depressor (Puritan) underneath the tail and taping the tail and the tongue depressor together using surgical tape. The catheter was flushed with 0.5% heparin in PBS to prevent clotting and secured with a stopper prior to contrast agent infusion.

Eight rats subsequently underwent ultrasound-mediated BBB disruption. Animals were maintained under 2% isoflurane anesthesia. Heads were shaved and cleaned with alcohol and povidone-iodine prep pads for easy access to the skull. The skin over the skull was retracted, and the skull was cleaned to visualize the coronal and sagittal sutures. Ultrasound transmission gel (Parker Aquasonic) was applied to the exposed skull.

An ultrasound transducer housing was then positioned in contact with the gel, with its center 1 mm above the skull and 2 mm lateral and 3 mm posterior to bregma. The housing was filled with circulating degassed and deionized water and was affixed to a custom transducer with 25-mm diameter and 500-kHz peak operating frequency (Sonic Concepts). Ultrasound waveforms were generated using a 25-MHz function generator (BK Precision) using the following settings: 500-kHz driving frequency, 0.2-V amplitude, 5,000 burst count, and 1-s burst rate. Waveforms were amplified using an ENI model 550L radio-frequency power amplifier (Bell Electronics) conditioned through an impedance matching network (Sonic Concepts) connected to the transducer itself.

Sonication was applied to each animal for 5 min. Immediately after the sonication was initiated, 50 μL of Optison microbubble ultrasound contrast agent (GE Healthcare) was injected through the tail vein catheter and flushed with 0.2 mL of 0.5% heparin in PBS. After sonication was completed, the skin was glued together using tissue glue, and the animal was immediately transferred to the MRI scanner for imaging.

Delivery and Imaging of Contrast Agents after BBB Disruption. Immediately after preparation, 12 rats (8 sonicated plus 4 unsonicated controls) were imaged during IV infusion of contrast agents. Each animal was maintained on 2% isoflurane in oxygen-enhanced air and placed into a custom-built cradle with a four-channel phased array coil (Bruker) fitting snugly over its head. Tail vein catheters were connected to tubing prefilled with SNIO or Gd-DTPA solutions, each 50 mM in metal ion concentration. Animals were then inserted into a 9.4-T MRI scanner (Bruker) equipped with a birdcage volume transmission coil (Bruker).

High-resolution T_2 -weighted anatomical scans of each animal were obtained using RARE pulse sequence with $TE = 56$ ms, $TR = 5,000$ ms, RARE factor 8, spatial resolution $156 \mu\text{m} \times 156 \mu\text{m} \times 1$ mm, and matrix size 128×128 with six slices. T_1 -weighted time series were then acquired using a RARE pulse sequence with $TE = 8.5$ ms, $TR = 680$ ms, spatial resolution $400 \mu\text{m} \times 400 \mu\text{m} \times 1$ mm, and matrix size 50×50 with six slices. Five minutes of baseline measurements with 30 s per time point were acquired before contrast agent infusion. MRI acquisition then continued at the same frame rate over a 5-min period, during which contrast agent was infused at a rate of 0.2 mL/min; this was followed by 20 min of continuing acquisition after infusion was completed. The estimated time between sonication and contrast agent delivery was 45 to 60 min.

The resulting MRI data were processed and analyzed using MATLAB and AFNI (National Institute of Mental Health) software packages. Brain data were segmented, aligned to a reference anatomical image, and normalized by setting each voxel's mean preinjection intensity to 100%. For calculating group-level signal change maps, voxels with significant delivery were

identified as those whose T_1 -weighted MRI signal was significantly above baseline during the 20-min period after contrast agent infusion was completed; significance was judged using a Student's t test over animals, with an uncorrected threshold of $P = 0.05$. Maps of mean signal change magnitude in these significant voxels were overlaid on anatomical MRI data. The signal change magnitudes were computed by comparing images obtained at 0 to 5 min (i.e., before contrast agent injection) vs. 25 to 30 min for Fig. 4C and by comparing images at 10 to 15 min (i.e., immediately postinjection) vs. 25 to 30 min for *SI Appendix*, Fig. S7. For purposes of judging mean contrast-enhanced volumes, voxels that experienced 1.5% signal change or greater from minute 10 to minute 30 time points were included. Time courses of signal change were generated by averaging percentage signal changes over 0.8-mm-radius spherical ROIs defined around peak signal change areas in the group dataset. SEs were calculated over animals.

Histopathology Analysis. To evaluate cytotoxicity after ultrasound-assisted SNIO brain delivery, animals were transcardially perfused with PBS followed by 4% paraformaldehyde in PBS. Brains were extracted, postfixed overnight at 4°C, and sectioned within a week. Tissue was rinsed with water and 100% ethanol in succession. Sections were then mounted onto glass slides and incubated in hematoxylin and eosin working solutions consecutively. Treated brain sections on glass slides were finally imaged by bright-field microscopy.

1. R. Weissleder, M. Nahrendorf, M. J. Pittet, Imaging macrophages with nanoparticles. *Nat. Mater.* **13**, 125–138 (2014).
2. H. B. Na, I. C. Song, T. Hyeon, Inorganic nanoparticles for MRI contrast agents. *Adv. Mater.* **21**, 2133–2148 (2009).
3. N. A. Frey, S. Peng, K. Cheng, S. Sun, Magnetic nanoparticles: Synthesis, functionalization, and applications in bioimaging and magnetic energy storage. *Chem. Soc. Rev.* **38**, 2532–2542 (2009).
4. N. Lee *et al.*, Iron oxide based nanoparticles for multimodal imaging and magneto-responsive therapy. *Chem. Rev.* **115**, 10637–10689 (2015).
5. J. Schnorr *et al.*, Cardiac magnetic resonance angiography using blood-pool contrast agents: Comparison of citrate-coated very small superparamagnetic iron oxide particles with gadofosveset trisodium in pigs. *RoFo Fortschr. Geb. Rontgenstr. Nuklearmed.* **184**, 105–112 (2012).
6. H. Wei *et al.*, Exceedingly small iron oxide nanoparticles as positive MRI contrast agents. *Proc. Natl. Acad. Sci. U.S.A.* **114**, 2325–2330 (2017).
7. Z. Kozakova *et al.*, The formation mechanism of iron oxide nanoparticles within the microwave-assisted solvothermal synthesis and its correlation with the structural and magnetic properties. *Dalton Trans.* **44**, 21099–21108 (2015).
8. T. Hyeon, S. S. Lee, J. Park, Y. Chung, H. B. Na, Synthesis of highly crystalline and monodisperse maghemite nanocrystallites without a size-selection process. *J. Am. Chem. Soc.* **123**, 12798–12801 (2001).
9. M. Zhang *et al.*, Size effects on magnetic properties of prepared by sol-gel method. *Adv. Mater. Sci. Eng.* **2013**, 10 (2013).
10. S. Neiser *et al.*, Physico-chemical properties of the new generation IV iron preparations ferumoxytol, iron isomaltoside 1000 and ferric carboxymaltose. *Biomaterials* **28**, 615–635 (2015).
11. M. V. Clavijo Jordan, S. C. Beeman, E. J. Baldeomar, K. M. Bennett, Disruptive chemical doping in a ferritin-based iron oxide nanoparticle to decrease r_2 and enhance detection with T_1 -weighted MRI. *Contrast Media Mol. Imaging* **9**, 323–332 (2014).
12. H. Wei *et al.*, Compact zwitterion-coated iron oxide nanoparticles for biological applications. *Nano Lett.* **12**, 22–25 (2012).
13. H. Wei, O. T. Bruns, O. Chen, M. G. Bawendi, Compact zwitterion-coated iron oxide nanoparticles for in vitro and in vivo imaging. *Integr. Biol.* **5**, 108–114 (2013).
14. C. H. Huang, A. Tsourkas, Gd-based macromolecules and nanoparticles as magnetic resonance contrast agents for molecular imaging. *Curr. Top. Med. Chem.* **13**, 411–421 (2013).
15. S. Okada *et al.*, Calcium-dependent molecular fMRI using a magnetic nanosensor. *Nat. Nanotechnol.* **13**, 473–477 (2018).
16. A. L. R. Xavier *et al.*, Cannula implantation into the cisterna magna of rodents. *J. Vis. Exp.* **135**, 57378 (2018).
17. A. Kirsherr, D. Franke, T. Kaulisch, D. Stiller, A. Briel, "Characterization of a novel gadolinium-based high molecular weight polymer as an intravascular MR contrast agent" in *International Society for Magnetic Resonance in Medicine 20th Annual Meeting* (International Society for Magnetic Resonance in Medicine Annual Meeting Proceedings, Melbourne, Australia, 2012), p. 1205.
18. H. J. Weinmann, R. C. Brasch, W. R. Press, G. E. Wesbey, Characteristics of gadolinium-DTPA complex: A potential NMR contrast agent. *AJR Am. J. Roentgenol.* **142**, 619–624 (1984).
19. Y. Huh, D. E. Smith, M. R. Feng, Interspecies scaling and prediction of human clearance: Comparison of small- and macro-molecule drugs. *Xenobiotica* **41**, 972–987 (2011).
20. M. D. Santin, T. Debeir, S. L. Bridal, T. Rooney, M. Dhenain, Fast in vivo imaging of amyloid plaques using μ -MRI Gd-staining combined with ultrasound-induced blood-brain barrier opening. *Neuroimage* **79**, 288–294 (2013).
21. G. P. Howles, Y. Qi, G. A. Johnson, Ultrasonic disruption of the blood-brain barrier enables in vivo functional mapping of the mouse barrel field cortex with manganese-enhanced MRI. *Neuroimage* **50**, 1464–1471 (2010).

Data Availability. All study data are included in the article and/or *SI Appendix*.

ACKNOWLEDGMENTS. A.W. was funded by the Advanced Multimodal Neuroimaging Training Program at the Massachusetts General Hospital through NIH Grant R90 DA023427. Y.L. and A.I.F. acknowledge support from NSF Grant DMR-1911592. A.M.F. was funded by the C. Michael Mohr Scholarship as awarded by the MIT Department of Chemical Engineering. This project was funded by an MIT Deshpande Center Innovation Grant (to M.G.B.) and NIH Grants R24 MH109081 (to A.J.), UF1 NS107712 (to A.J.), and R01 DA038642 (to A.J.). This work also benefited from the use of the SasView application, originally developed under NSF Award DMR-0520547. SasView contains code developed with funding from the European Union's Horizon 2020 Research and Innovation Programme under Science and Innovation with Neutrons in Europe 2020 (SINE2020) Project Grant 654000. This research used beamline 7-BM (Quick X-ray Absorption and Scattering, QAS) of the National Synchrotron Light Source II, a Department of Energy (DOE) Office of Science User Facility operated by Brookhaven National Laboratory under Contract DE-SC0012704. Beamline operations were supported in part by the Synchrotron Catalysis Consortium (DOE Office of Basic Energy Sciences Grant DE-SC0012335). We thank Oliver Bruns for helpful discussions, Yong Zhang and Patrick Boisvert for help with TEM and SQUID magnetometry, Jiahao Huang for help with X-ray absorption fine structure measurements, and Athena Ortega and Francisco Acosta for assistance with MATLAB scripts.

22. D. E. J. Waddington, T. Boele, R. Maschmeyer, Z. Kuncic, M. S. Rosen, High-sensitivity in vivo contrast for ultra-low field magnetic resonance imaging using superparamagnetic iron oxide nanoparticles. *Sci. Adv.* **6**, eabb0998 (2020).
23. J. Wahsner, E. M. Gale, A. Rodriguez-Rodriguez, P. Caravan, Chemistry of MRI contrast agents: Current challenges and new frontiers. *Chem. Rev.* **119**, 957–1057 (2019).
24. M. D. Sweeney, A. P. Sagare, B. V. Zlokovic, Blood-brain barrier breakdown in Alzheimer disease and other neurodegenerative disorders. *Nat. Rev. Neurol.* **14**, 133–150 (2018).
25. A. Abraham *et al.*, First-in-human trial of blood-brain barrier opening in amyotrophic lateral sclerosis using MR-guided focused ultrasound. *Nat. Commun.* **10**, 4373 (2019).
26. J. R. Reichenbach *et al.*, $1H$ T_1 and T_2 measurements of the MR imaging contrast agents Gd-DTPA and Gd-DTPA BMA at 1.5T. *Eur. Radiol.* **7**, 264–274 (1997).
27. L. Bokacheva *et al.*, Quantitative determination of Gd-DTPA concentration in T_1 -weighted MR renography studies. *Magn. Reson. Med.* **57**, 1012–1018 (2007).
28. A. Barandov *et al.*, Sensing intracellular calcium ions using a manganese-based MRI contrast agent. *Nat. Commun.* **10**, 897 (2019).
29. A. Barandov *et al.*, Molecular magnetic resonance imaging of nitric oxide in biological systems. *ACS Sens.* **5**, 1674–1682 (2020).
30. B. H. Kim *et al.*, Large-scale synthesis of uniform and extremely small-sized iron oxide nanoparticles for high-resolution T_1 magnetic resonance imaging contrast agents. *J. Am. Chem. Soc.* **133**, 12624–12631 (2011).
31. L. Wang *et al.*, Exerting enhanced permeability and retention effect driven delivery by ultrafine iron oxide nanoparticles with T_1 - T_2 switchable magnetic resonance imaging contrast. *ACS Nano* **11**, 4582–4592 (2017).
32. T. Todd *et al.*, Iron oxide nanoparticle encapsulated diatoms for magnetic delivery of small molecules to tumors. *Nanoscale* **6**, 2073–2076 (2014).
33. G. Yi, J. Son, J. Yoo, C. Park, H. Koo, Application of click chemistry in nanoparticle modification and its targeted delivery. *Biomater. Res.* **22**, 13 (2018).
34. Q. Mu *et al.*, Anti-HER2/neu peptide-conjugated iron oxide nanoparticles for targeted delivery of paclitaxel to breast cancer cells. *Nanoscale* **7**, 18010–18014 (2015).
35. M. Zhao *et al.*, A GPC3-specific aptamer-mediated magnetic resonance probe for hepatocellular carcinoma. *Int. J. Nanomedicine* **13**, 4433–4443 (2018).
36. H. T. Ta *et al.*, Molecular imaging of activated platelets via antibody-targeted ultra-small iron oxide nanoparticles displaying unique dual MRI contrast. *Biomaterials* **134**, 31–42 (2017).
37. J. Perez-Rodriguez, S. Lai, B. D. Eht, D. M. Fine, D. A. Bluemke, Nephrogenic systemic fibrosis: Incidence, associations, and effect of risk factor assessment—report of 33 cases. *Radiology* **250**, 371–377 (2009).
38. R. J. McDonald *et al.*, Intracranial gadolinium deposition after contrast-enhanced MR imaging. *Radiology* **275**, 772–782 (2015).
39. T. Kanda *et al.*, High signal intensity in dentate nucleus on unenhanced T_1 -weighted MR images: Association with linear versus macrocyclic gadolinium chelate administration. *Radiology* **275**, 803–809 (2015).
40. M. Auerbach, G. M. Chertow, M. Rosner, Ferumoxytol for the treatment of iron deficiency anemia. *Expert Rev. Hematol.* **11**, 829–834 (2018).
41. T. Rieker, A. Hanprasopwattana, A. Datye, P. Hubbard, Particle size distribution inferred from small-angle X-ray scattering and transmission electron microscopy. *Langmuir* **15**, 638–641 (1999).
42. W. Szczerba, R. Costo, S. Veintemillas-Verdaguer, M. D. Morales, A. F. Thünemann, SAXS analysis of single- and multi-core iron oxide magnetic nanoparticles. *J. Appl. Cryst.* **50**, 481–488 (2017).
43. B. R. Pauw, C. Kästner, A. F. Thünemann, Nanoparticle size distribution quantification: Results of a small-angle X-ray scattering inter-laboratory comparison. *J. Appl. Cryst.* **50**, 1280–1288 (2017).